EDGE ARTICLE

Check for updates

All publication charges for this article have been paid for by the Royal Society of Chemistry

Chelation-regulated release of alloying species stabilizes electrochemical interfaces on metal anodes in batteries

Rustam K. Gandhi, [ID] [a] Sydney Manning[a] and J. X. Kent Zheng [ID] *[abc]

Functional additives are widely used in electrochemical systems to guide metal deposition and suppress unfavorable porous growth modes. A key strategy involves adding secondary metal cations with higher redox potentials, which spontaneously undergo ion exchange and deposit as an interfacial alloying layer to promote uniform growth during battery recharge. However, we discover that in the absence of kinetic control, this electroless deposition of the alloying layer unexpectedly induces dendritic growth due to local ion depletion, especially when additive concentrations are low. Contrary to conventional wisdom, free additive cations can therefore destabilize—rather than stabilize—metal anode interfaces. To overcome this, we introduce a chelation-based approach that regulates the release of additive cations and smooths interfacial deposition. Using Cu^{2+} additives and EDTA chelators in aqueous Zn batteries as a model system, we demonstrate that chelation enables controlled Cu^{2+} release, forming uniform interfacial layers and remarkably improving cycling stability. The chelation-regulated system achieves >99% Zn reversibility and 2–3× longer cycle life under practical current densities and capacities (*i.e.*, 1 mAh cm^{-2} at 10 mA cm^{-2}, and 10 mAh cm^{-2} at 10 mA cm^{-2}), while unregulated systems fail rapidly. Extension of the controlled release framework to systems beyond the Cu^{2+}–EDTA pair is also demonstrated. This work highlights the importance of molecular-level control over additive reactivity and offers a generalizable strategy for stabilizing metal anodes in energy-dense batteries.

Electrochemical deposition of metals, *i.e.*, $M_{(solution)}^{n+} + ne^- \rightarrow M_{(solid)}$, has long been an industrially important process, used in applications such as semiconductor microfabrication, surface finishing, and electrowinning.[1–3] Most recently, electrodeposition gained further momentum due to its critical role in batteries featuring high-energy-density metal anodes. Unfortunately, in all these electrodeposition processes, the formation of porous, sometimes "dendritic" deposits is a persistent challenge.[4,5] The porosity can arise from a variety of factors, including the diffusion limit of the metal cations and the heterogeneity of the passivating interphase.[6–9] In battery electrodes, these porous growth patterns are extremely problematic; it not only introduces structural fragility leading to the formation of "dead" metal fragments, but also pose a significant risk of internal short-circuiting, leading to fatal cell failure.[10–12]

Small quantities of additives are commonly introduced to electrolytes used in electrochemical systems.[13] In batteries, an important class of additives consists of secondary metal cations

M_B^{m+} with a redox potential higher than the primary metal M_A used in the cell, *i.e.*, $\Phi_{M_B^{m+}/M_B} > \Phi_{M_A^{n+}/M_A}$. Upon contact, the metallic M_A anode and the M_B^{m+} cations in the solution undergo a spontaneous ion exchange reaction: $nM_B^{m+} + mM_A \rightarrow nM_B + mM_A^{n+}$. This spontaneous reaction results in the electroless deposition of M_B on the surface of the anode made of M_A (Fig. S1a). Through alloying with M_A, this thin M_B layer is anticipated to reduce the nucleation energy barrier ΔG^* and therefore promote uniform electrochemical growth of M_A in the subsequent cycling (Fig. S1b). For example, Cu^{2+} has been identified as a candidate secondary metal cation for Zn metal anodes,[14–16] and Ag^+ for Li metal anodes.[17,18] In addition to incorporating additives into the electrolyte, such approaches were also extensively used for *ex situ* pretreatment of the metal anodes forming the M_B layer prior to battery assembly.[19–21] See Table S1 for more literature reports. In these cases where M_B^{m+} is used as an additive to create a conformal M_B layer, its concentration $C_{M_B^{m+}}$ is typically on the order of 10 mM or below 1 wt%.

A careful assessment of the electroless deposition of M_B from a mass transport perspective, however, suggests otherwise. Compared to a concentrated electrolyte (typically ~1 M), a dilute electrolyte makes M_B^{m+} highly susceptible to depletion near the deposition interface where it is continuously

[a]Department of Chemical Engineering, University of Texas at Austin, Austin, Texas 78712, USA. E-mail: kentz@utexas.edu

[b]Texas Materials Institute, University of Texas at Austin, Austin, Texas 78712, USA

[c]Bard Center for Electrochemistry, University of Texas at Austin, Austin, Texas 78712, USA

consumed and converted into M_B. This cation depletion is known to be the origin of classical diffusion-limited dendritic growth patterns. Such diffusion-limited dendritic growth has been observed in a variety of systems—both electroless or electrochemical—including nanocrystal growth,[22–24] particle self-assembling,[25] and metal deposition.[6,26] In particular, this phenomenon has been examined in-depth both theoretically and experimentally in the context of electrochemical deposition, as dendrites can lead to fatal failure modes in electrochemical cells. It is well established that the balance between the reaction rate—often quantified by the exchange current density J_0, which is proportional to standard reaction rate constant k_0—and the mass transport rate dictates the system's susceptibility to diffusion-limited dendritic growth.[27,28] When the chemical reaction rate at the interface far exceeds the mass transport rate in the liquid electrolyte, steep concentration gradients $\nabla C_{M_B^{m+}}$ develop, driving dendritic growth. A similar analysis should be applicable to electroless growth of M_B.[29–31] This hypothesis is significant as it suggests that the electroless growth of functional metal M_B itself exhibits a highly porous, dendritic nature, introducing substantial chemical and morphological heterogeneity to the M_A metal surface. These additional undesirable heterogeneities now introduced upon the electrode surface, in theory, serve as "hot spots" for non-uniform or even dendritic growth of M_A during subsequent electrodeposition;[32,33] see Fig. 1a for an example with Zn and Cu as M_A and M_B, respectively.

The central hypothesis that motivates this work is that—analogous to drug delivery, where a sudden large dosage can lead to unfavorable consequences—a regulated release mechanism is necessary for functional M_B^{m+} species to promote uniform and stable M_A deposition upon battery cycling. Specifically in electrochemical cells, the regulated release mechanism should significantly reduce the chemical reaction rate of the electroless M_B deposition, thereby suppressing steep $\nabla C_{M_B^{m+}}$ gradients and mitigating dendritic growth. Common controlled-release strategies for drug deliveries—such as polymer encapsulation and liposome/micelles encapsulation—often involve complex chemical procedures to fabricate microcapsules containing the functional additives.[34,35] Moreover, the impact of these encapsulating agents with complex chemistries on electrochemical processes remains largely unknown.

Given these constraints with encapsulation-based strategies, we further hypothesize that chelation—a simple chemical binding interaction between M_B^{m+} cations and a coordinating molecule—can be used to achieve controlled release of M_B^{m+}. The chelation of M_B^{m+} is expected to significantly decrease the reaction rate for the electroless reduction of M_B^{m+} to M_B, by introducing an additional de-chelation step prior to the electroless deposition. Therefore, the chemical reaction rate can be moderated such that is commensurate to the rate of mass transport to avoid the formation of steep $\nabla C_{M_B^{m+}}$ gradients and dendritic growth (Fig. 1b). We define two key screening criteria for an ideal chelating agent to enable controlled release of M_B^{m+}. First, the chelating agent should exhibit highly selective
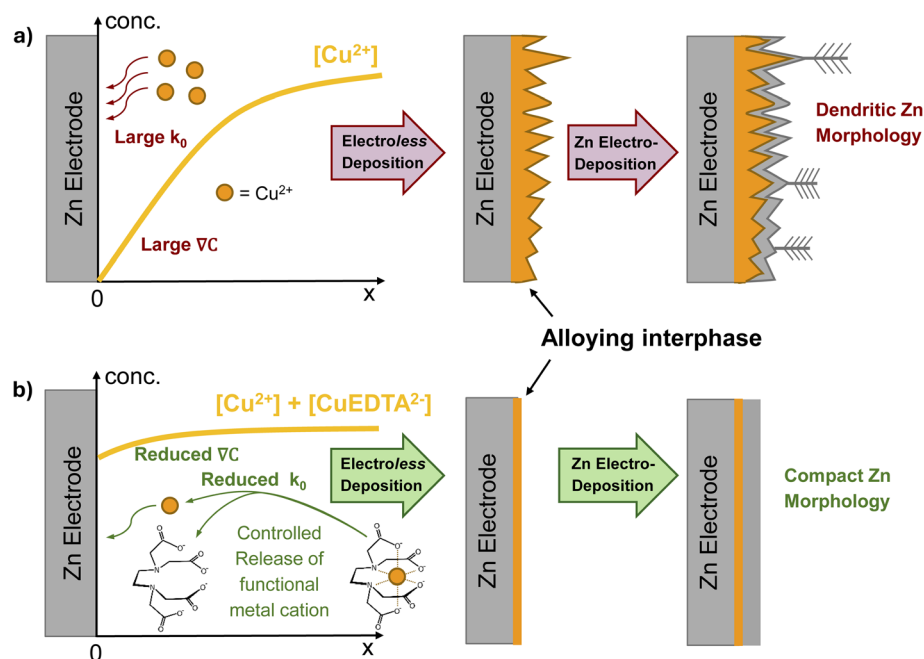

Fig. 1 Release of alloying species and its impact on interfacial properties of metal anodes. (a) Schematic diagram showing the formation of a functional layer *via* the unregulated electroless deposition of Cu²⁺. The layer is non-uniform due to the diffusion-limited growth mode of Cu. It follows that Zn electrodeposition upon this heterogeneous layer will also be heterogeneous. (b) Schematic diagram showing the formation of a functional layer when Cu²⁺ electroless deposition is regulated by the controlled release mechanism. The additional kinetic barrier of the de-chelation step ensures the reaction rate is kinetically limited, leading to compact Cu morphology. The uniform functional layer allows for compact Zn electrodeposition to follow.

binding with M_B^{m+} rather than with M_A^{n+}, since the primary conducting salt in the electrolyte M_A^{n+} exists in large quantities. Second, the chelating agent must also be compatible with all other components and processes occurring within the electrochemical cell.

As a model system to validate our hypotheses and proposed approach, we focus on Zn metal anodes with mildly acidic aqueous electrolytes. The selection is motivated by its immediate technological relevance to large-scale sustainable energy storage, and several additional fundamental considerations. Unlike alkali-metal anodes, which form highly passivating interphases that strongly influence all interfacial processes, Zn exhibits less passivating behavior. This allows us to directly investigate how the *in situ* formation and morphology of M_B influences the growth of M_A. Moreover, the alloying chemistry between Zn and secondary elements is well studied. For example, our previous work using a variety of thick commercial M_B foils demonstrated that a Sabatier-like principle governs alloy-involved deposition processes, with Cu emerging as the optimal alloying element (*i.e.*, M_B) for Zn.[36]

In choosing an effective chelating agent for the controlled release of Cu^{2+} in the Zn electrolyte, we first evaluate the formation constant K_f of several common complexing/chelating agents with Cu^{2+}; we then compare these values to the K_f for Zn^{2+}. See Table S2. To ensure that chelation predominantly occurs with Cu^{2+} instead of Zn^{2+}, an ideal chelating agent should exhibit a K_f for Cu^{2+} at least two orders of magnitude greater than for Zn^{2+}. Ethylenediaminetetraacetic acid disodium salt (EDTA-Na$_2$) stands out as an optimal choice due to its strong selective binding with Cu^{2+} $\left(\frac{K_f(\text{EDTA} - Cu^{2+})}{K_f(\text{EDTA} - Zn^{2+})} = 1.7 \times 10^2 \right)$ and its compatibility with the mildly acid environment. EDTA has been demonstrated as an effective agent for achieving smooth electrochemical Cu deposition in aqueous environments,[37,38] and EDTA-based salts have been explored as a functional additive for pure Zn^{2+} electrolyte in the absence of Cu^{2+}.[39] By contrast, candidates such as ammonia, NH_3 and ethylenediamine, $H_2NCH_2CH_2NH_2$, exhibit significant basicity, which is less favorable in the mildly acidic Zn electrolyte. Furthermore, the complexing strength weakens as the $-NH_2$ becomes protonated under mildly acidic conditions. Taking these analyses together, we hypothesize that EDTA is an effective chelating agent for the controlled release of Cu^{2+} in Zn metal anodes.

Results and discussion

Chelation-regulated release of functional species

The chelation of the primary cation M_A^{n+} and the secondary function cation M_B^{m+} is competitive, especially given the high concentration of M_A^{n+} in the electrolyte. In this specific system, while the formation constant (K_f) for Cu^{2+} is two orders of magnitude greater than that for Zn^{2+}, it is not straightforward to determine the precise concentration of the chelating agent required to ensure that the majority of Cu^{2+} remains in the chelated state for effective controlled release. To address this,

we leverage the characteristic UV-Vis spectroscopic response of Cu^{2+}, which provides insight into its coordination state, to ascertain the necessary chelating agent concentration. Specifically, we examine the UV-Vis spectrum of a 1 M $ZnSO_4$ electrolyte containing 20 mM $CuSO_4$ while varying the EDTA concentration (Fig. 2a). The EDTA-to-Cu^{2+} molar ratio is adjusted across four conditions: no EDTA (0:1), EDTA deficient (1:10, 1:4, 1:2), stoichiometric equivalence (1:1), and excess EDTA (10:1). Without EDTA, the solution exhibits an absorbance peak at 809 nm, which can be attributed to the t_{2g} to e_g transition of the $Cu(H_2O)_6^{2+}$ complex ion.[40] Upon the addition of EDTA, we observe a significant blue shift of the peak towards 742 nm, accompanied by a five-fold increase in absorbance. The blue shift is expected due to the greater crystal field splitting Δ induced by EDTA chelation.[41] The strong enhancement of the absorbance, on the other hand, can be attributed to the broken inversion symmetry in the EDTA–Cu^{2+} chelate, permitting otherwise forbidden d–d transitions, according to the Laporte rule. We observe that the maximum blue shift and absorbance is attained when the concentration of EDTA equals or exceeds the Cu^{2+} concentration. In order to ensure that the maximum fraction of Cu^{2+} is chelated at all times, we select a molar ratio of 10:1 throughout the remainder of this work.

Quantitatively, reaction kinetics are best described by the standard rate constant k_0; however, its experimental determination is challenging. We wish to probe the electroless deposition rate of Cu, which cannot be measured directly with standard electrochemical techniques. Furthermore, in a diffusion-limited regime, any experimentally measured reaction rate is largely governed by mass transport, rather than by intrinsic chemical kinetics. To overcome these challenges, we configure an electrochemical setup for Cu electrodeposition (as a proxy for the electroless reaction) onto an inert glassy carbon substrate and measure the exchange current density J_0 well below the diffusion limited regime. A discussion on the relationship between electro- and electroless deposition kinetics is provided at the end of this section.

It is well established that J_0 and k_0 are linearly related by $J_0 = nFk_0C_{Cu^{2+}}^{1-\beta}$, where n is the number of electrons transferred, F is Faraday constant and β is the symmetry factor. This relationship implies that a substantial reduction in k_0 of the electroless reaction kinetics should be directly reflected as a decrease in J_0, which we measure electrochemically in the kinetics-dominated regime, away from diffusion limitations. Linear sweep voltammetry (LSV) was performed in 1 M $ZnSO_4$ + 20 mM $CuSO_4$ solutions with various concentrations of EDTA (Fig. S2). The resulting Tafel plot is shown in Fig. 2b. The y-intercept of the linear region represents the logarithm of the exchange current density, which decreases significantly as EDTA concentration increases (or, equivalently, as Cu^{2+} free ion concentration decreases). In fact, J_0 is decreased by roughly 35% when 200 mM EDTA is present (0.674 *vs.* 0.436 mA cm^{-2}, respectively). The same experiment is performed in a 500 mM Na_2SO_4 + 20 mM $CuSO_4$ electrolyte, where Na_2SO_4 replaces $ZnSO_4$ as the supporting electrolyte (Fig. S3). The formation constant for the Na–EDTA complex is 16 orders of magnitude lower than that of Cu–EDTA and 14 orders of magnitude lower
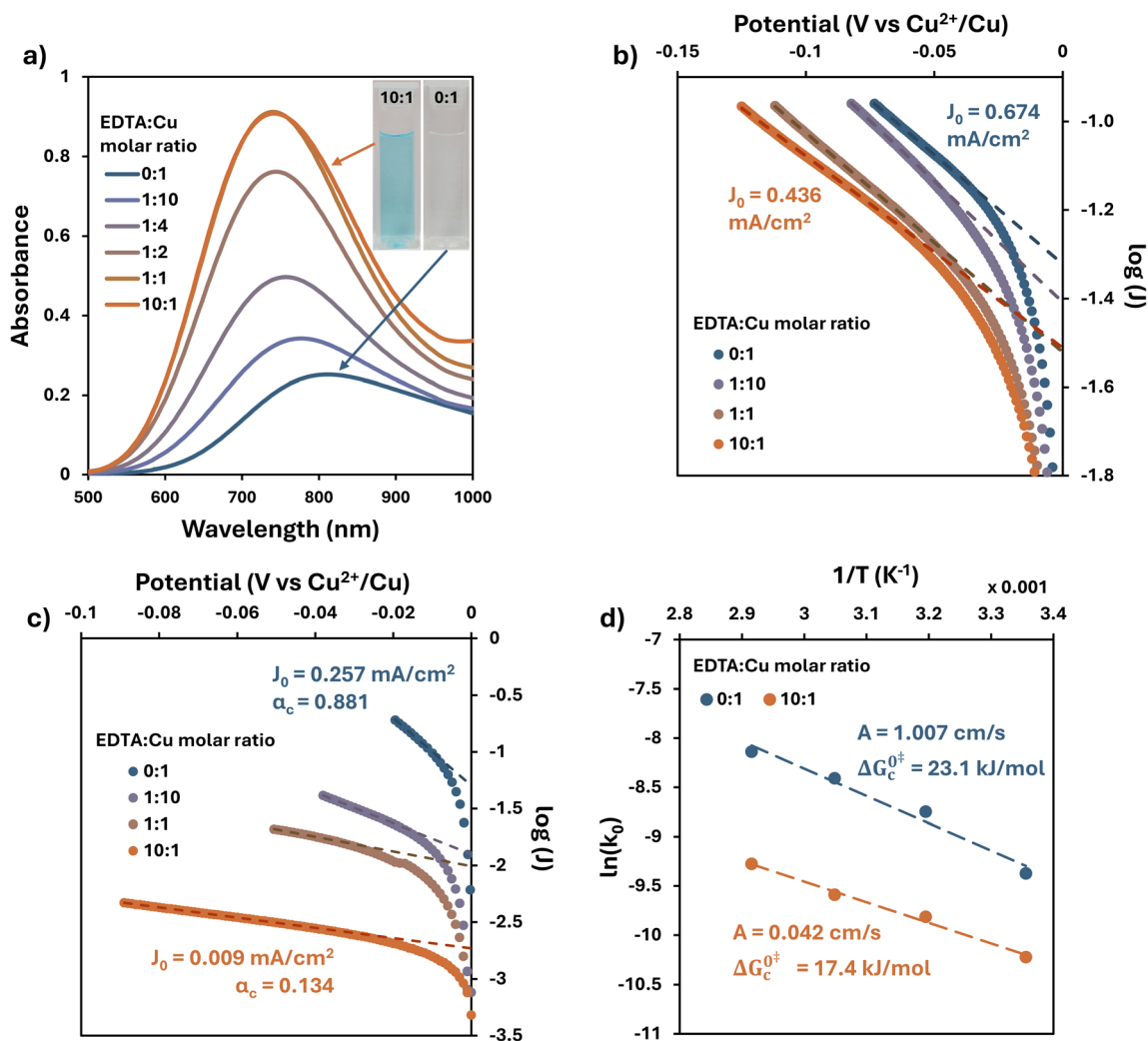
Fig. 2 Understanding Cu^{2+} chelation and its effects on reaction kinetics. (a) UV-Vis absorbance spectra of a 1 M $ZnSO_4$ + 20 mM $CuSO_4$ electrolyte as the EDTA : Cu^{2+} ratio is increased. Tafel plots measuring Cu^{2+} electrodeposition kinetics from a 1 M $ZnSO_4$ + 20 mM $CuSO_4$ electrolyte (b), and a 500 mM Na_2SO_4 + 20 mM $CuSO_4$ electrolyte (c), as the EDTA : Cu^{2+} ratio is increased. (d) Arrhenius plot of Cu electrodeposition kinetics at a variety of temperatures, from a 0.2 M Na_2SO_4 + 20 mM $CuSO_4$ electrolyte with and without 200 mM EDTA. The working electrode is glassy carbon and the scan rate is 20 mV s^{-1} for all measurements.

than that of Zn–EDTA; thus, the extent of Cu^{2+} chelation in this system is increased.[42] The Tafel plot (Fig. 2c) reveals that a 10 : 1 EDTA : Cu^{2+} solution decreases J_0 tenfold when Cu^{2+} chelation is not competitive, demonstrating the extraordinary extent to which the controlled release phenomenon can suppress the standard rate constant for electroless deposition.

Further insight into the reaction mechanism for Cu deposition from the EDTA-containing electrolyte can be gleaned from temperature-dependent kinetic measurements. LSV is performed in 200 mM Na_2SO_4 + 20 mM $CuSO_4$ electrolytes with and without 200 mM EDTA at various temperatures (Fig. S4). The data is highly linear when plotted as $\ln(k_0)$ *vs.* $1/T$, according to the Arrhenius equation $k_0 = A \exp\left(-\dfrac{\Delta G_c^{0\ddagger}}{RT}\right)$, with r^2 values of 0.991 and 0.974 with and without EDTA, respectively (Fig. 2d). Note that such an Arrhenius plot captures only the behavior of the system in the absence of an overpotential (*i.e.*, $\eta = 0$), since

J_0 and k_0 measure the equilibrium reaction rates, by definition.[43] Therefore, the slope of the Arrhenius plot is related to $\Delta G_c^{0\ddagger}$, or the activation energy of the electrodeposition reaction in the absence of an overpotential (this quantity is indicated schematically in Fig. S5). From these fits, the calculated activation energies $\Delta G_c^{0\ddagger}$ are on the same order of magnitude: 17.4 kJ mol^{-1} and 23.1 kJ mol^{-1} for the cases with and without EDTA, respectively. However, it is the preexponential factor A that differs significantly upon the addition of EDTA. Without EDTA, the preexponential factor is 1.007 cm s^{-1}. Once EDTA is added, however, the preexponential factor decreases by approximately 1.4 orders of magnitude to 0.042 cm s^{-1}. Physically, the preexponential factor represents the collision frequency (in this case, the frequency of Cu^{2+}–electrode interactions), whereas the exponential term $\exp\left(-\dfrac{\Delta G_c^{0\ddagger}}{RT}\right)$

represents the fraction of these collisions with sufficient energy to trigger the reaction. The decrease in the preexponential factor indicates fewer Cu^{2+} ions are free to interact with the electrode surface, as most are complexed with the EDTA. Those that are complexed cannot be reduced until de-chelation occurs. The similar activation energies suggest that once de-chelation occurs, the Cu^{2+} ions behave similarly to those in the EDTA-free electrolyte. This interpretation strongly suggests a two-step mechanism for Cu^{2+} reduction from the EDTA-containing electrolyte:

$$CuEDTA^{2-} \rightleftharpoons Cu^{2+} + EDTA^{4-} \tag{E1}$$

$$Cu^{2+} + 2e^- \rightarrow Cu_0 \tag{E2}$$

In the absence of an overpotential, the first reaction (E1) is in equilibrium, dictated by the formation constant K_f of the $CuEDTA^{2-}$ complex. Since the value of K_f is large (5×10^{18}), the equilibrium lies far towards the reactants of reaction (E1). Thus, the concentration of free Cu^{2+} ions available for reduction in reaction (E2) is remarkably small (compared to the EDTA-free electrolyte), which explains the reduced preexponential factor. Chelation, then, is directly responsible for the decrease in the electrodeposition rate *via* a greater-than-tenfold reduction of the preexponential factor, providing irrefutable evidence for the controlled release mechanism.

We also observe that EDTA reduces the magnitude of the cathodic charge transfer coefficient α_c, which is directly proportional to the slopes of the Tafel curves in Fig. 2c. Notably, upon the addition of EDTA, α_c is decreased from 0.881 to 0.134, and the anodic charge transfer coefficient α_a is correspondingly increased ($1 - \alpha_c = \alpha_a$). That is to say, the kinetics for the cathodic Cu deposition reaction becomes more sluggish, due to the necessity of the de-chelation step, but the propensity for the reverse anodic Cu dissolution is increased. See Fig. S5 for a detailed discussion.

From the above analyses, it is evident that the introduction of EDTA to the electrolyte significantly reduces the Cu electrodeposition kinetics. However, it is prudent to establish the relationship between the electro- and electroless deposition kinetics, as it is the latter which is of highest importance to this work. The reaction between M_A and M_B is a galvanic displacement reaction,[44] since the more noble M_B deposits on the surface while the less noble M_A dissolves over the course of the reaction. This system can be analyzed from the framework of mixed potential theory, often used to study corrosion processes.[45] Fig. S6 shows the Evans diagram for the galvanic displacement reaction between Zn and Cu. Both the reduction in J_0 and α_c caused by EDTA are shown schematically, and the result is a suppressed corrosion current, or electroless deposition rate (see Fig. S6 for a complete discussion). Thus, measurements of M_B deposition kinetics under electrochemical conditions are explicitly related to M_B electroless deposition rates.

Stabilizing electroless and electrochemical interfaces

To investigate the effect of chelation-regulated release Cu^{2+} on the electroless deposition morphology of Cu, we examine the surface of a Zn foil after 2 hours immersion in a 1 M $ZnSO_4$ + 20 mM $CuSO_4$ solution, in the absence and presence of 200 mM EDTA, respectively; see schematic diagram in Fig. S7. The foils immersed in the EDTA-free electrolyte appear matte and black, suggesting mossy or dendritic growth associated with nanoporosity;[46–48] in stark contrast, those immersed in the EDTA-containing electrolyte appear shiny and "coppery" in color, indicating a compact morphology (inset of Fig. 3a and b).[49,50] Of note is that the black coloration observed is consistent with prior literature reports on electroless Cu deposition without controlled release mechanisms, suggesting the anticipated porosity.[19,20] Scanning electron microscopy (SEM) characterization of the surfaces confirms these hypotheses (Fig. 3c, d and S8). The functional layer from the EDTA-free electrolyte exhibits large, non-uniform features and non-compact growth normal to the plane of the substrate, which eventually evolves into highly dendritic patterns after longer immersion (Fig. S9). The functional layer created in the EDTA electrolyte shows a comparatively compact, smooth surface, devoid of large non-uniform features.

Optical profilometry quantifies this difference: the unregulated functional layer has a surface roughness threefold higher than what is obtained from the EDTA electrolyte (Fig. 3c and d). Focused ion-beam milling (FIB) was used to prepare cross sections of the electroless Cu layers (Fig. 3e and f). The cross sections and related electron dispersive spectroscopy (EDS) mappings (Fig. 3g and h) directly reveal the mossy nature of the functional layer when EDTA is absent. Additionally, the interface between the bulk Zn metal and the deposited layer contains many small voids, whereas the same interface has nearly perfect contact when EDTA is used. This explains the difference in mechanical integrity between the two functional layers—the matte black layer can be easily scraped and scratched by a pair of tweezers, while the shiny golden layer is much more mechanically robust (Fig. S10); additional cross sections and more detailed discussion can be found in Fig. S11. This set of surface morphology characterizations confirms the critical role played by chelation-regulated release in promoting a favorable, conformal electroless deposition morphology of M_B.

For completeness, we examine the possibility that native surface inhomogeneities on the Zn electrode play a significant role in determining the electroless deposition morphology, since the Zn foils were used as received. An electropolishing procedure described in our previous work is performed to minimize any inherent spatial variation on the Zn surface.[51] The electropolished foil was then subjected to the same electroless deposition procedure used thus far (Fig. S7). The resulting morphology (Fig. S12) is qualitatively no different from those in Fig. 3a and b. We thus conclude that any morphological differences observed follow directly from the electrolyte chemistry, and not from any inherent spatial inhomogeneities on the Zn electrode.
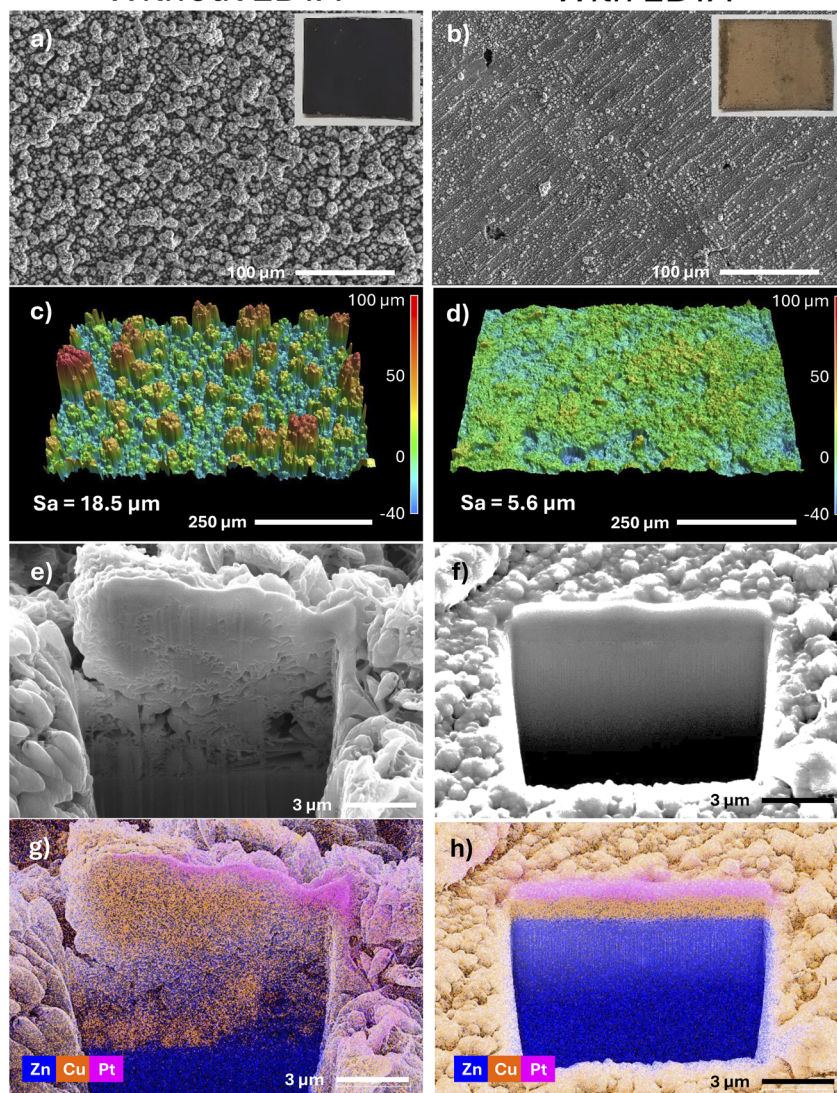
Fig. 3 Effect of chelation-regulated release on the properties of the alloying layer. SEM and optical (inset) images of the functional layer created without (a) and with (b) EDTA after 2 hours immersion. (c and d) 3D profile from optical profilometry measurements of the functional layer after 24 hours immersion. (e and f) FIB-SEM cross sections of the interface after 2 hours immersion, and their corresponding EDS maps (g and h). A protective Pt layer is deposited onto the sample before the cross section is milled. Electrolyte: 1 M $ZnSO_4$ + 20 mM $CuSO_4$, or 1 M $ZnSO_4$ + 20 mM $CuSO_4$ + 200 mM EDTA.

As a final step in validating our central hypothesis, we now investigate the impact of chelation on the electrodeposition morphology of M_A. We performed electrodeposition of Zn in a 1 M $ZnSO_4$ + 20 mM $CuSO_4$ solution, in the absence and presence of 200 mM EDTA, upon their respective functional layers (Fig. S13). The SEM images (Fig. 4a, b and S14) and profilometry measurements (Fig. 4c and d) show marked differences. The deposited layer in the EDTA-free electrolyte is highly dendritic, with large tree-like structures and smaller "hopper crystals" present across the sample.[52] In stark contrast, the surface of the deposited layer in the EDTA-containing electrolyte is extraordinarily uniform, with a clear absence of large-scale heterogeneities. In fact, the surface roughness is reduced by an order of magnitude when EDTA is included in the electrolyte. The uniformity is increased compared to Zn deposition without any functional layer as well (Fig. S15). FIB cross sections and EDS mappings corroborate these observations. Without EDTA, Zn is forced to deposit on and around the non-uniform Cu protrusions, which are visible in the cross section. The total height of the functional and deposited layers together is approximately 6 μm. However, when EDTA is added, the layers are far more compact, and the total height is only 3 μm. It is worth noting that the Cu protrusions into the deposited layer are of different origins in each case. In Fig. 4g, the origin is

Deposited Layer
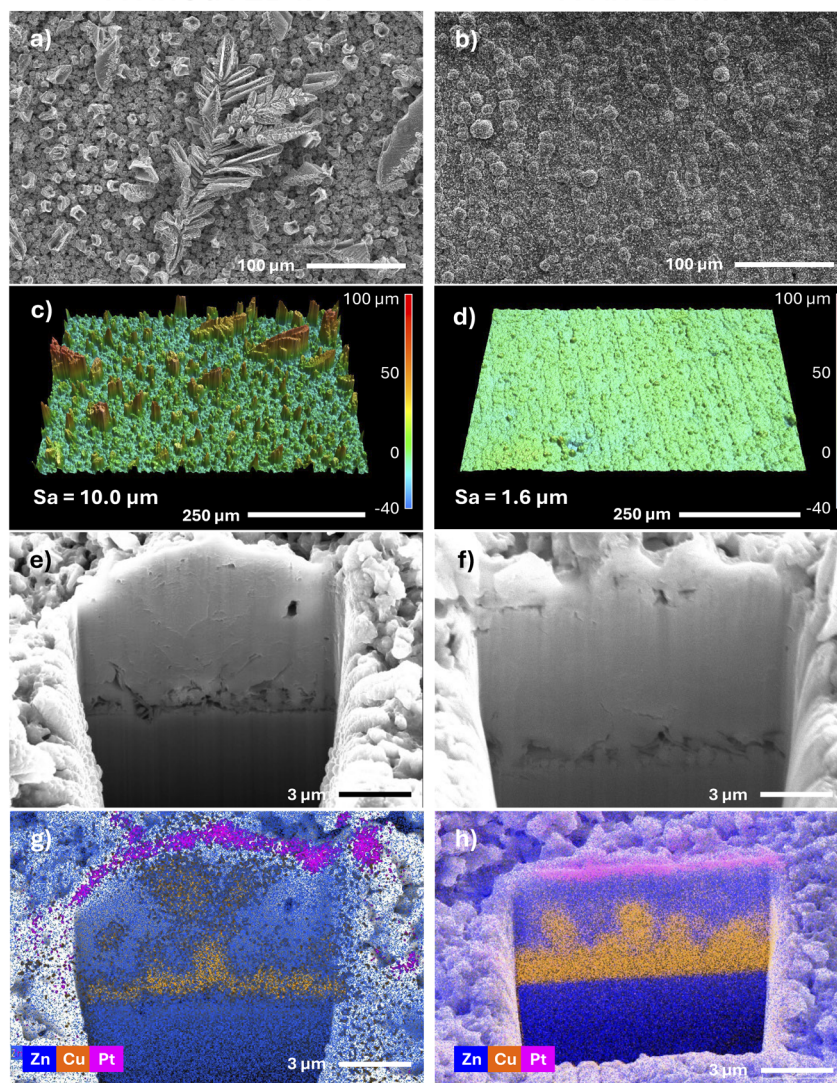## *Without EDTA*   *With EDTA*

Fig. 4 Zn electrodeposition on the alloying layer. SEM images of Zn electrodeposition from electrolyte without (a) and with (b) EDTA, upon the respective functional layer. (c and d) 3D profile from optical profilometry measurements of the Zn deposits. (e and f) FIB–SEM cross sections of the interface after Zn deposition, and their corresponding EDS maps (g and h). Electrolyte: 1 M $ZnSO_4$ + 20 mM $CuSO_4$, or 1 M $ZnSO_4$ + 20 mM $CuSO_4$ + 200 mM EDTA. Zn deposition performed at 10 mA cm^{-2} and 5 mAh cm^{-2}. A protective Pt layer is deposited onto the sample before the cross section is milled by FIB.

likely from the porous nature of the functional layer itself, as suggested by Fig. 3g. However, we hypothesize that the bulbous Cu shapes observed in Fig. 4h are likely a result of Cu diffusion from the functional layer into the Zn deposited layer (see Fig. S16 for a detailed discussion), since no such features are visible before Zn deposition in Fig. 3h. Clearly, the electrodeposition morphology achieved through chelation-regulated release exhibits significantly improved surface uniformity and reduced surface roughness. These results highlight the exceptional interfacial stability in both electroless and electrochemical metal growth, enabled by the regulated-release mechanism.

Probing interfacial alloying phenomena

Driven by the unconventional compact electrodeposition morphology achieved through the controlled-release strategy, we employ complementary structural and chemical characterization techniques to gain insights into the interfacial alloying process. X-ray diffraction (XRD) measurements elucidate the phases present in the functional (Fig. 5a) and deposited layers (Fig. 5b).[53] In all cases, peaks from pure Zn are observed (Fig. S17). Examining the patterns of the functional layers, a broad shoulder on the left side of the $(101)_{Zn}$ peak at $2\theta = 44°$ ($d = 2.05$ Å) is discernible when the EDTA is present; this shoulder at a smaller 2θ value might be attributed to $(111)_{Cu}$

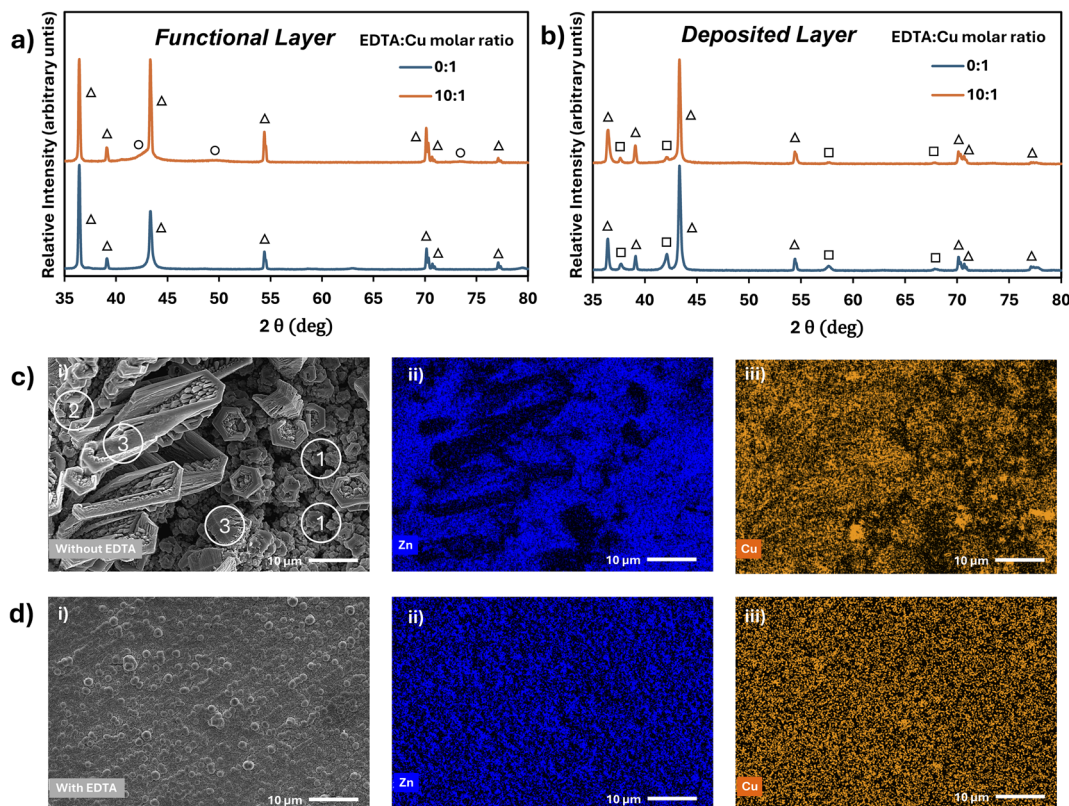Fig. 5 Interfacial alloying mechanisms of electrodeposited Zn. XRD patterns ($\triangle$ -Zn; $\bigcirc$ -Cu; $\square$ -CuZn$_5$) of the functional layers (a) and the Zn deposits upon these layers (b). SEM images and corresponding Zn and Cu EDS maps of the deposited layer without (c) and with (d) EDTA.

with a slightly larger interplanar spacing $d = 2.07$ Å. This shoulder is absent when EDTA is excluded, suggesting that the Cu deposits are either more porous/nano-structured or poorer in crystallinity, and therefore are not represented in the pattern. Turning to the diffraction patterns of the deposited layers, we again observe that pure metallic Cu is absent. Instead, in both cases, the remaining peaks are assigned to an intermetallic phase composed of Cu and Zn in a 1 : 5 ratio.[54–57] Therefore, all the Cu present in the deposited layer is incorporated into this alloy phase. The intensity of the alloy peaks is reduced when controlled release is in place. Because the electrolyte contains Cu^{2+}, freshly deposited Zn on the functional layer will spontaneously react with Cu^{2+} in solution, as observed previously. The extent of this reaction is mitigated by EDTA, resulting in a lower Cu content in the deposited layer. This observation is further corroborated by the EDS spectra (Fig. S18) of the mappings: the relative counts of Cu decreased by a factor of 4 when the Cu^{2+}-chelating agent is present.

We performed additional EDS mappings to discover the spatial distribution of the phases identified from XRD. Fig. 5c shows the EDS mappings of sections of the images in Fig. 4a. The section of the EDTA-free case is highly heterogeneous and complex; it contains the edge of a large dendritic structure on the left, and the surrounding deposits on the right. From the mapping, three regions can be broadly identified: (1) those with strong Zn signal but weaker Cu signal, (2) those with strong Zn and Cu signal, and (3) those with weaker Zn signal but stronger

Cu signal. We hypothesize that regions matching the profile of (1) suggest pure Zn deposits, giving rise to the pure Zn peaks in the XRD pattern, while region (2) likely represents the intermetallic phase. The assignment of region (3) is less straightforward, but we attribute it to a solid solution, where additional Cu has been dissolved into the intermetallic phase. This may explain the fact that the intermetallic peaks in the XRD pattern appear slightly broader than the Zn peaks. Interestingly, we note that the regions with higher Cu content, *i.e.*, region (3), seem to be prominent at the "extremities" or tips of the dendritic structures (the few intense "hot-spots" in the Cu map are excluded from this observation, as they are likely measuring the functional layer at points where the deposited layer is incomplete). Though the mechanisms behind this observation are beyond the scope of this work, we attribute this difference to the mass-transport-induced gradient in Cu^{2+} concentration, such that the large protruding dendritic growth extends a significant distance into the diffusion layer, where the rate of the ion exchange reaction is larger.

In stark contrast, the EDS maps for the regulated-release case show far less spatial differentiation, especially in the Cu map, which shows a uniformly weak signal across the entire area (Fig. 5d). We suggest that regions (1) and (2) are present, but not (3), in accordance with the reasoning presented above. The complementary characterization results of the interfacial alloying processes suggest that the controlled release of the functional M_B^{m+} promotes its uniform incorporation into the

M_A layer upon electrochemical deposition and a compact morphology.

Enabling cycling stability under stringent conditions

Motivated by the observed interfacial stability enabled by the controlled release strategy, we assess its influence on the electrochemical plating/stripping reversibility in coin-type batteries. Coulombic Efficiency (CE) measurements with an inert stainless steel substrate (configuration: Zn‖SS) were performed in three different electrolytes: 1 M $ZnSO_4$, 1 M $ZnSO_4$ + 20 mM $CuSO_4$, and 1 M $ZnSO_4$ + 20 mM $CuSO_4$ + 200 mM EDTA. The selected current density of 10 mA cm^{-2} was intentionally aggressive to probe the reversibility in harsh conditions, while the plated capacities tested varied from moderate (1 mAh cm^{-2})

to harsh (10 mAh cm^{-2}) (Fig. 6a and b, respectively). In this scenario, the Cu^{2+} ions in the electrolyte serve two distinct roles: they deposit as metallic Cu on the stainless steel substrate upon application of current, directly affecting the CE; they also spontaneously react with the Zn foil to form a Cu functional layer as described above, which influences the cycle life of the cell. With only $ZnSO_4$, the nucleation barrier is large, ~100 mV (Fig. 6c). Upon the addition of $CuSO_4$, the barrier is reduced to ~30 mV. However, when the electrolyte contains both $CuSO_4$ and EDTA, the nucleation barrier is removed altogether. It follows that, based on the reasoning in Fig. S1b, the Cu + EDTA + Zn electrolyte showed the best reversibility, with CEs remaining higher than 98% for >50 cycles at high capacity and >1000 cycles at low capacity.
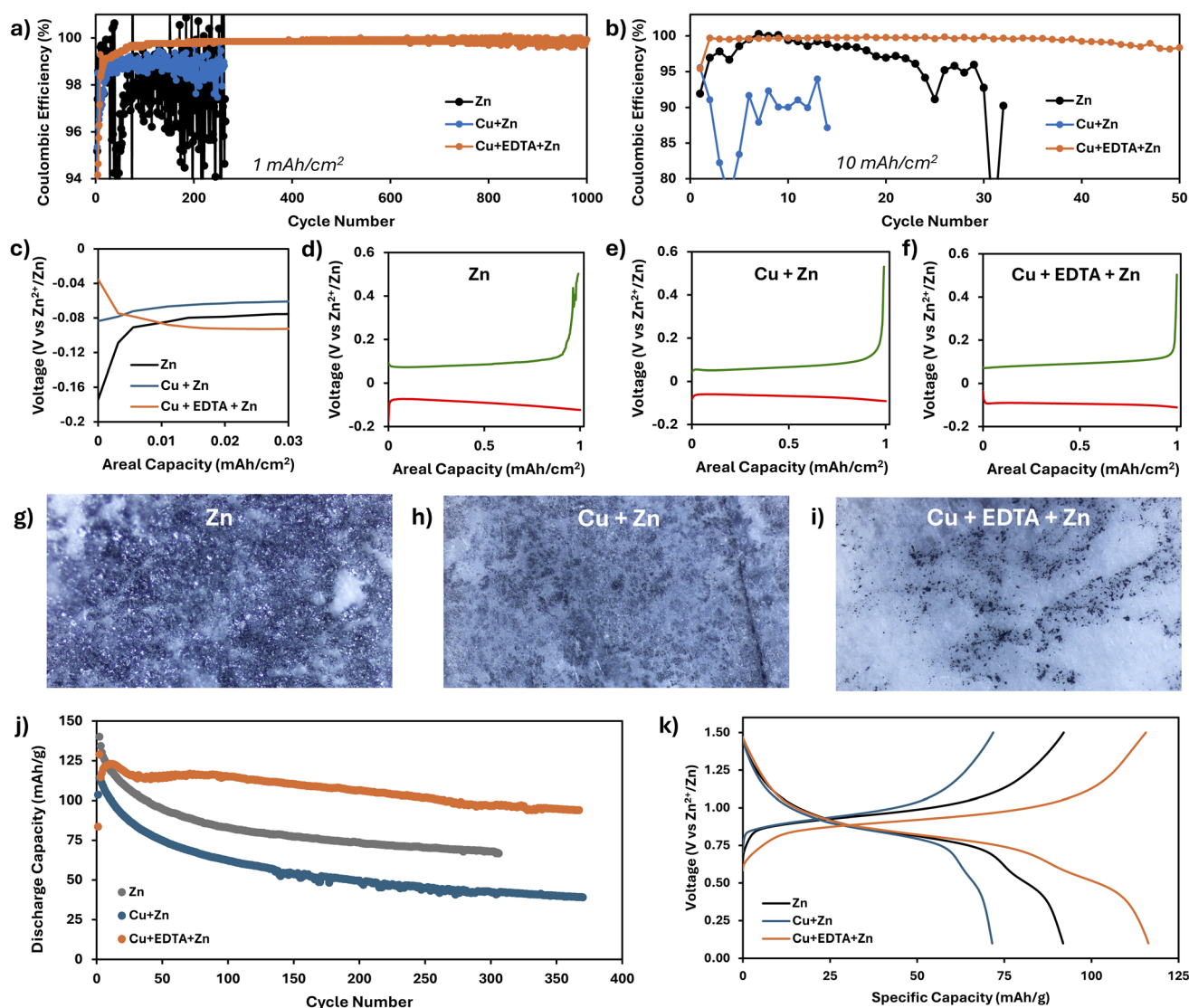

Fig. 6 Electrochemical stability and performance enabled by controlled release of alloying species. Coulombic efficiency of Zn plating/stripping over a large number of cycles at 1 mAh cm^{-2} (a) and 10 mAh cm^{-2} (b). Capacity–voltage profile during nucleation (c) and during cycling in 1 M $ZnSO_4$ (d), 1 M $ZnSO_4$ + 20 mM $CuSO_4$ (e), and 1 M $ZnSO_4$ + 20 mM $CuSO_4$ + 200 mM EDTA (f) electrolytes. Optical microscopy images of the separator after 100 cycles at 1 mAh cm^{-2} in these electrolytes (g–i). The current density was 10 mA cm^{-2} for all measurements. (j) Full cell (Zn–NVO) discharge capacities as a function of cycle life. The discharge capacity is normalized by the NVO loading. (k) Representative charge–discharge voltage profiles (cycle # 60) of Zn–NVO cells. Cells are cycled between 0.1 and 1.5 V vs. Zn^{2+}/Zn at 1 mA cm^{-2}.

The full voltage profiles corroborate this observation. Features distinctly suggestive of metal orphaning are observed in the 1 M ZnSO$_4$ electrolyte. Indeed, the irregularities in the voltage trace during stripping (Fig. 6d) suggest the random and unpredictable disconnection and reconnection of dead metal fragments. This same phenomenon explains how the coulombic Efficiency is greater than 100% for some cycles in Fig. 6a. The separator facing the stainless steel plating/stripping surface was imaged with optical microscopy after ∼100 cycles at low capacity, revealing substantial orphaned metal fragments in the 1 M ZnSO$_4$ and 1 M ZnSO$_4$ + 20 mM CuSO$_4$ cases (Fig. 6g and h, respectively). However, in the Cu + EDTA + Zn electrolyte, the amount of dead metal on the separator is significantly reduced (Fig. 6i).

Under harsh conditions (high capacity), the Cu–Zn electrolyte performed significantly worse than even the pure Zn electrolyte. Clearly, the heterogeneities of the functional and deposited layers arising from an unregulated functional metal cation only exacerbate the low intrinsic CE of Zn. In fact, the amount of dead metal on the Cu–Zn separator is greater than that on the 1 M ZnSO$_4$ separator under these conditions (Fig. S19).

To rule out the possibility that the presence of EDTA itself, rather than its interaction with Cu^{2+}, leads to the observed improvement, we also measure the CE with 1 M ZnSO$_4$ + 200 mM EDTA, in the absence of Cu^{2+}. The performance is found to be comparably poor (Fig. S20), similar to the baseline 1 M ZnSO$_4$ electrolyte.

Finally, we construct coin cells with Zn anodes, paired with sodium vanadate (NVO) cathodes[58] to examine the cycling stability enabled by the controlled release mechanism in a full cell configuration. The same Zn, Cu + Zn, and Cu + EDTA + Zn electrolytes were used, as described above. The results in Fig. 6j are in good agreement with the symmetric cell results (Fig. 6a and b), where the best performance is achieved from the Cu + EDTA + Zn electrolyte, and the additional heterogeneity stemming from the unregulated Cu + Zn electrolyte leads to worse performance than even the pure ZnSO$_4$ control. A representative charge–discharge voltage profile is shown in Fig. 6k, where it is clear that the charging overpotential for the controlled release case is significantly lower than that from the unregulated and control electrolytes. This is likely due to the absence of a significant nucleation barrier, as shown in Fig. 6c. The comparison of these coin-type battery results decisively confirms the critical role played by the interaction between the functional metal cation and the chelating agent—*i.e.*, is, the chelation-regulated release—in enabling extraordinary cycling stability in battery anodes.

Extending the controlled release framework to other M$_A$/M$_B$ systems

Given the success of the controlled release strategy in the Cu/Zn system demonstrated in this work, we briefly show the application of chelation-regulated electroless deposition in other technologically relevant scenarios. Specifically, we replace M$_B^{m+}$ with Ag$^+$. As with Cu, spontaneous Ag deposition on Zn exhibits highly dendritic morphology when unregulated due to the evolution of steep concentration gradients. Electroless Ag deposition is carried out as in Fig. S7 from a 20 mM AgNO$_3$ electrolyte. Fig. S21 clearly shows tree-like and faceted dendritic structures arising from diffusion-limited growth after only 10 minutes immersion of a Zn foil in a 20 mM AgNO$_3$ electrolyte. Like with Cu, EDTA can regulate Ag deposition morphology by significantly reducing the rate of the Ag deposition reaction (Fig. S22). Consistent with the controlled release framework, SEM images in Fig. S23 show more uniform substrate coverage without large dendrites. With success in both Cu and Ag systems, EDTA demonstrates the reliability of chelation as an effective control mechanism, showing effectiveness at multiple time scales and with multiple M$_B^{m+}$. Indeed, this strategy should be universally applicable in any system where the chelator has a high relative affinity for M$_B^{m+}$.

Conclusion

Designing electrolyte chemistry and controlling interfacial chemical kinetics have been key areas of exploration for enabling energy-dense metal anodes. Contrary to conventional wisdom, our findings reveal that, when the dilute secondary functional metal cation M$_B^{m+}$ additive exists in its free form, it surprisingly leads to highly porous and dendritic patterns, primarily due to its susceptibility to diffusion limitations. A rationally designed controlled-release strategy is essential to gradually release the functional ions, allowing the formation of a compact alloy layer that promotes interfacial stability in subsequent electrochemical deposition. Chelation is demonstrated as an effective strategy for such controlled release in electrochemical cells. In particular, we define two screening criteria for identifying an ideal chelating agent: high selectivity for chelation with the secondary functional cation M$_B^{m+}$ over the primary salt cation M$_A^{n+}$, and compatibility with battery components and processes. Using EDTA-regulated release of Cu^{2+} in Zn metal anodes as an example, we demonstrate the crucial role that controlled release plays in achieving uniform growth and stable cycling under practical operating conditions. Taken together, these results provide important insights for rational molecular-level engineering of critical additives and open a new avenue for enabling highly reversible metal anodes in batteries.

Author contributions

K. Z. directed the research. R. K. G. and K. Z. conceived and designed this work. R. K. G. and S. M. performed the electrochemical measurements and materials characterization. R. K. G., S. M., and K. Z. analyzed the data. R. K. G., S. M., and K. Z. wrote the paper.

Conflicts of interest

There are no conflicts to declare.

Data availability

The data supporting this article have been included as part of the SI. See DOI: https://doi.org/10.1039/d5sc04189a.

Acknowledgements

References

1 K. Popov, B. Grgur and S. S. Djokić, *Fundamental aspects of electrometallurgy*, Springer, 2007.

2 P. C. Andricacos, Copper on-chip interconnections: a breakthrough in electrodeposition to make better chips, *Electrochem. Soc. Interface*, 1999, **8**(1), 32.

3 N. Krishnamurthy and C. K. Gupta, *Miner. Process. Extr. Metall. Rev.*, 2002, **22**(4–6), 477–507.

4 R. Akolkar, Modeling dendrite growth during lithium electrodeposition at sub-ambient temperature, *J. Power Sources*, 2014, **246**, 84–89.

5 S. J. Banik and R. Akolkar, Suppressing dendritic growth during alkaline zinc electrodeposition using polyethylenimine additive, *Electrochim. Acta*, 2015, **179**, 475–481.

6 J. Zheng, J. Yin, D. Zhang, G. Li, D. C. Bock, T. Tang, *et al.*, Spontaneous and field-induced crystallographic reorientation of metal electrodeposits at battery anodes, *Sci. Adv.*, 2020, **6**(25), eabb1122.

7 J. X. K. Zheng, J. Yin, T. Tang and L. A. Archer, Moss-like growth of metal electrodes: on the role of competing faradaic reactions and fast charging, *ACS Energy Lett.*, 2023, **8**(5), 2113–2121.

8 P. Bai, J. Li, F. R. Brushett and M. Z. Bazant, Transition of lithium growth mechanisms in liquid electrolytes, *Energy Environ. Sci.*, 2016, **9**(10), 3221–3229.

9 B. Ma and P. Bai, Fast charging limits of ideally stable metal anodes in liquid electrolytes, *Adv. Energy Mater.*, 2022, **12**(9), 2102967.

10 C. Fang, J. Li, M. Zhang, Y. Zhang, F. Yang, J. Z. Lee, *et al.*, Quantifying inactive lithium in lithium metal batteries, *Nature*, 2019, **572**(7770), 511–515.

11 J. Zheng, T. Tang, Q. Zhao, X. Liu, Y. Deng and L. A. Archer, Physical orphaning versus chemical instability: is dendritic electrodeposition of Li fatal?, *ACS Energy Lett.*, 2019, **4**(6), 1349–1355.

12 J. X. K. Zheng, Perspective—Reversibility of Electro-Plating/Stripping Reactions: Metal Anodes for Rechargeable Batteries, *J. Electrochem. Soc.*, 2022, **169**(10), 100532.

13 H. Zhang, G. G. Eshetu, X. Judez, C. Li, L. M. Rodriguez-Martínez and M. Armand, Electrolyte additives for lithium metal anodes and rechargeable lithium metal batteries: progress and perspectives, *Angew. Chem., Int. Ed.*, 2018, **57**(46), 15002–15027.

14 J. Peng, J. Yu, D. Chu, X. Hou, X. Jia, B. Meng, *et al.*, Synergistic effects of an artificial carbon coating layer and Cu^{2+}-electrolyte additive for high-performance zinc-based hybrid supercapacitors, *Carbon*, 2022, **198**, 34–45.

15 M. Zhou, Z. Wu, R. Wang, G. Sun and S.-Q. Zang, An in situ reduction strategy toward dendrite-free Zn anodes, *Sci. China Mater.*, 2023, **66**(5), 1757–1766.

16 G. Yang, K. Ma and C. Wang, Unconventional copper electrochemistry in aqueous Zn‖$CuMn_2O_4$ batteries, *Adv. Energy Mater.*, 2024, **14**(12), 2303695.

17 Q. Wang, D. Yang, W. Xin, Y. Wang, W. Han, W. Yan, *et al.*, Modulation of desolvation barriers and inhibition of lithium dendrites based on lithophilic electrolyte additives for lithium metal anode, *Chin. Chem. Lett.*, 2024, 110669.

18 P. Zhai, N. Ahmad, S. Qu, L. Feng and W. Yang, A lithiophilic–lithiophobic gradient solid electrolyte interface toward a highly stable solid-state polymer lithium metal batteries, *Adv. Funct. Mater.*, 2024, **34**(27), 2316561.

19 C. Liu, Q. Lu, A. Omar and D. Mikhailova, A facile chemical method enabling uniform Zn deposition for improved aqueous Zn-ion batteries, *Nanomaterials*, 2021, **11**(3), 764.

20 Y. Chen, Q. Zhao, Y. Wang, W. Liu, P. Qing and L. Chen, A dendrite-free $Zn@Cu_xZn_y$ composite anode for rechargeable aqueous batteries, *Electrochim. Acta*, 2021, **399**, 139334.

21 Y. Zhang, Q. Chen, D. Li, S. Qi, Y. Liu, J. Liu, *et al.*, AgTFSI Pretreated Li Anode in LiI-Mediated $Li\text{-}O_2$ Battery: Enabling Lithiophilic Solid Electrolyte Interphase Generation to Suppress the Redox Shuttling, *CCS Chem.*, 2024, **6**(10), 2400–2410.

22 B. Lim and Y. Xia, Metal nanocrystals with highly branched morphologies, *Angew. Chem., Int. Ed.*, 2011, **50**(1), 76–85.

23 S. Liu, X. Liu, L. Xu, Y. Qian and X. Ma, Controlled synthesis and characterization of nickel phosphide nanocrystal, *J. Cryst. Growth*, 2007, **304**(2), 430–434.

24 Y.-H. Liu, C.-J. Hsieh, L.-C. Hsu, K.-H. Lin, Y.-C. Hsiao, C.-C. Chi, *et al.*, Toward controllable and predictable synthesis of high-entropy alloy nanocrystals, *Sci. Adv.*, 2023, **9**(19), eadf9931.

25 A. Sukhanova, A. V. Baranov, T. S. Perova, J. H. M. Cohen and I. Nabiev, Controlled Self-Assembly of Nanocrystals into Polycrystalline Fluorescent Dendrites with Energy-Transfer Properties, *Angew. Chem., Int. Ed.*, 2006, **45**(13), 2048–2052.

26 C. M. López and K.-S. Choi, Electrochemical synthesis of dendritic zinc films composed of systematically varying motif crystals, *Langmuir*, 2006, **22**(25), 10625–10629.

27 D. A. Cogswell, Quantitative phase-field modeling of dendritic electrodeposition, *Phys. Rev. E: Stat., Nonlinear, Soft Matter Phys.*, 2015, **92**(1), 011301.

28 Y. Liu, X. Xu, M. Sadd, O. O. Kapitanova, V. A. Krivchenko, J. Ban, *et al.*, Insight into the critical role of exchange current density on electrodeposition behavior of lithium metal, *Adv. Sci.*, 2021, **8**(5), 2003301.

29 X. Wen, Y.-T. Xie, W. C. Mak, K. Y. Cheung, X.-Y. Li, R. Renneberg, *et al.*, Dendritic nanostructures of silver: facile synthesis, structural characterizations, and sensing applications, *Langmuir*, 2006, **22**(10), 4836–4842.

30 W.-F. Cai, K.-B. Pu, Q. Ma and Y.-H. Wang, Insight into the fabrication and perspective of dendritic Ag nanostructures, *J. Exp. Nanosci.*, 2017, **12**(1), 319–337.

31 A. Kuhn and F. Argoul, Diffusion-limited kinetics in thin-gap electroless deposition, *J. Electroanal. Chem.*, 1995, **397**(1–2), 93–104.

32 Y. Hu, Z. Li, Z. Wang, X. Wang, W. Chen, J. Wang, *et al.*, Suppressing local dendrite hotspots via current density redistribution using a superlithiophilic membrane for stable lithium metal anode, *Adv. Sci.*, 2023, **10**(12), 2206995.

33 D. Han, X. Wang, Y. N. Zhou, J. Zhang, Z. Liu, Z. Xiao, *et al.*, A graphene-coated thermal conductive separator to eliminate the dendrite-induced local hotspots for stable lithium cycling, *Adv. Energy Mater.*, 2022, **12**(25), 2201190.

34 T.-W. Lim, C. W. Park, S. R. White and N. R. Sottos, Time release of encapsulated additives for enhanced performance of lithium-ion batteries, *ACS Appl. Mater. Interfaces*, 2017, **9**(46), 40244–40251.

35 M. Machtakova, H. Thérien-Aubin and K. Landfester, Polymer nano-systems for the encapsulation and delivery of active biomacromolecular therapeutic agents, *Chem. Soc. Rev.*, 2022, **51**(1), 128–152.

36 J. Zheng, Y. Deng, W. Li, J. Yin, P. J. West, T. Tang, *et al.*, Design principles for heterointerfacial alloying kinetics at metallic anodes in rechargeable batteries, *Sci. Adv.*, 2022, **8**(44), eabq6321.

37 N. N. Che Isa, Y. Mohd, M. H. Mohd Zaki and S. A. Syed Mohamad, Electrodeposition and characterization of copper coating on stainless steel substrate from alkaline copper solution containing ethylenediaminetetraacetate (EDTA), *J. Mech. Eng.*, 2017, (1), 127–138.

38 X. Song, C. Wang, D. Wang, H. Peng, C. Wang, C. Wang, *et al.*, Electrolyte additive enhances the electrochemical performance of Cu for rechargeable Cu//Zn batteries, *J. Energy Chem.*, 2023, **77**, 172–179.

39 J. Cao, D. Zhang, R. Chanajaree, Y. Yue, Z. Zeng, X. Zhang, *et al.*, Stabilizing zinc anode via a chelation and desolvation electrolyte additive, *Adv. Powder Mater.*, 2022, **1**(1), 100007.

40 D. Puchalska, G. Atkinson and S. Routh, Solution thermodynamics of first-row transition elements. 4. Apparent molal volumes of aqueous $ZnSO_4$ and $CuSO_4$ solutions from 15 to 55 °C, *J. Solution Chem.*, 1993, **22**, 625–639.

41 D. C. Bowman, A colorful look at the chelate effect, *J. Chem. Educ.*, 2006, **83**(8), 1158.

42 D. C. Harris, *Quantitative chemical analysis*, Macmillan, 2010.

43 A. J. Bard, L. R. Faulkner and H. S. White, *Electrochemical methods: fundamentals and applications*, John Wiley & Sons, 2022.

44 S. S. Djokić and N. S. Djokić, Electroless deposition of metallic powders, *J. Electrochem. Soc.*, 2011, **158**(4), D204.

45 W. S. Tait, Electrochemical corrosion basics, *Handbook of environmental degradation of materials*, Elsevier, 2018, pp. 97–115.

46 B. Yu, Y. Wang, Y. Zhang and Z. Zhang, Self-supporting nanoporous copper film with high porosity and broadband light absorption for efficient solar steam generation, *Nano-Micro Lett.*, 2023, **15**(1), 94.

47 B. Yu, Y. Wang, Y. Zhang and Z. Zhang, Nanoporous black silver film with high porosity for efficient solar steam generation, *Nano Res.*, 2023, **16**(4), 5610–5618.

48 Y. Zhang, Y. Wang, B. Yu, K. Yin and Z. Zhang, Hierarchically structured black gold film with ultrahigh porosity for solar steam generation, *Adv. Mater.*, 2022, **34**(21), 2200108.

49 Y.-C. Liao and Z.-K. Kao, Direct writing patterns for electroless plated copper thin film on plastic substrates, *ACS Appl. Mater. Interfaces*, 2012, **4**(10), 5109–5113.

50 B. Satpathy, S. Jena, S. Das and K. Das, Theoretical and experimental studies of mirror-bright Au coatings deposited from a novel cyanide-free thiosulphate-based electroplating bath, *Surf. Coat. Technol.*, 2023, **453**, 129149.

51 S. T. Fuller and J. X. K. Zheng, On the hidden transient interphase in metal anodes: dynamic precipitation controls electrochemical interfaces in batteries, *Proc. Natl. Acad. Sci. U. S. A.*, 2025, **122**(15), e2425752122.

52 P. C. Bollada, P. K. Jimack and A. M. Mullis, Phase field modelling of hopper crystal growth in alloys, *Sci. Rep.*, 2023, **13**(1), 12637.

53 S. Gražulis, D. Chateigner, R. T. Downs, A. F. T. Yokochi, M. Quirós, L. Lutterotti, *et al.*, Crystallography Open Database – an open-access collection of crystal structures, *Appl. Crystallogr.*, 2009, **42**(4), 726–729.

54 Z. Wang, K. Wang, X. Zhu, Z. Huang, D. Chen, S. Sun, *et al.*, Establishing copper-zinc alloying strategy via active screen plasma toward stabilized zinc metal anode, *EcoMat*, 2023, **5**(5), e12328.

55 J.-M. Song, Y.-L. Shen and H.-Y. Chuang, Sedimentation of Cu-rich intermetallics in liquid lead-free solders, *J. Mater. Res.*, 2007, **22**(12), 3432–3439.

56 *Effect of Al Content on Microstructure and Properties of Zn-Cu-Al Alloy*, ed. H. Wang, Y. Zhang, C. Wang, S. Cao, W. Bai and C. Wu, *et al.*, IOP Publishing, 2020.

57 G. Li, Y. Gao, S. Liu, Z. Wang, S. Liu and Q. Wang, Microstructural evolution of the oxidized ZnO:Cu films tuned by high magnetic field, *J. Alloys Compd.*, 2018, **753**, 673–678.

58 F. Wan, L. Zhang, X. Dai, X. Wang, Z. Niu and J. Chen, Aqueous rechargeable zinc/sodium vanadate batteries with enhanced performance from simultaneous insertion of dual carriers, *Nat. Commun.*, 2018, **9**(1), 1656.